Bi-functional two-dimensional cobalt silicate catalyst for selective catalytic oxidation of ammonia

Siyeon Lee [a,1], Sang Woo Byun [b,1], Sungjoon Kweon [a], Hyeonwoo Shin [b], Hyung-Ki Min [c], Min Bum Park [a,*], Sung Bong Kang [b,d,**]

[a] Department of Energy and Chemical Engineering, Incheon National University, Incheon 22012, Korea
[b] School of Earth Sciences and Environmental Engineering, Gwangju Institute of Science and Technology, Gwangju 61005, Korea
[c] Lotte Chemical Research Institute, Daejeon 34110, Korea
[d] Research Center for Innovative Energy and Carbon Optimized Synthesis for Chemicals(Inn-ECOSysChem), Gwangju Institute of Science and Technology, Gwangju 61005, Korea

ABSTRACT

We have newly synthesized the zeolitic cobalt silicate catalysts via a simple hydrothermal treatment of boro-silicate MWW precursor with Co precursor solution. As the hydrothermal temperature increased, a structural transformation occurred, shifting from three-dimensional (3D) to two-dimensional (2D) delaminated MWW layers (DML), and further to 2D amorphous phyllosilicate, accompanied by a continuous increase in Co content. The synthesized bi-functional 2D cobalt silicate facilitates the selective catalytic oxidation of NH_3 (NH_3-SCO), a process that requires both surface acidity and redox characteristics. In particular, Co-DML-160 prepared by hydrothermal treatment at 160 °C exhibited the coexistence of Co_3O_4 and framework Co species resulting in a strong redox ability and high Lewis acidity, respectively, due to their synergetic effect.

1. Introduction

A catalyst is a critical material that lowers the activation energy to accelerate chemical reactions and enhances the selectivity toward the desired end products [1]. Among the various factors determining catalytic performance, the nature of active sites is one of the most important aspects for developing efficient catalysts in diverse chemical reactions. Typically, three representative characteristics have been suggested as the efficient catalytic active sites: Metal for (de)hydrogenation, metal oxide for redox reaction, and acid/base for cracking reaction [2–4]. Recently, modern bi-functional catalysts that possess more than two distinct types of active sites have gained significant attention due to their ability to efficiently handle different elementary steps in an overall chemical reaction, resulting in the optimal selectivity for desired products [5]. For example, Cu-ZnO-Al₂O₃/Zr-modified ferrierite zeolite (framework type FER) showed a promising CO conversion of ~50% with the dimethylether selectivity ~58% from synthesis gas thanks to the reducibility of Cu species and the mild acidity of Zr-ferrierite support [6].

The selective catalytic oxidation of ammonia (NH_3-SCO) enables the reduction of unreacted NH_3, known as NH_3 slip in the selective catalytic reduction of NH_3 (NH_3-SCR), transforming it into N_2 through the main reaction: $4NH_3 + 3O_2 \rightarrow 2N_2 + 6H_2O$ [7]. Two primary functionalities have been investigated in the development of a high-performance NH_3-SCO catalyst: redox ability and surface acidity, which are required for oxidizing NH_3 and the chemisorption of NH_3, respectively [8,9]. For instance, Jabłońska et al. reported that optimally impregnated Pd (1.5%) on HY zeolite (FAU, Si/Al = 2.6) catalysts exhibited high Pd dispersion due to the high surface area of HY [10]. The synergic effect of this highly dispersed Pd, which contributes to redox ability and the acidity of HY, which aids in the chemisorption of NH_3, improved the high NH_3 conversion and N_2 selectivity. In addition, Ag/SiO₂–TiO₂ catalyst demonstrated improved NH_3-SCO performance compared to Ag/SiO₂ or Ag/TiO₂, as evidenced by a significantly lower T_{90}, the temperature at which 90% conversion is achieved. This improvement can be attributed to the beneficial effects of the reducibility from Ag^0 and surface acidity provided by the TiO₂ support [11].

Metallosilicates have been proposed as potential candidate catalysts

---

in numerous oxidation reactions leveraging their characteristic acidity derived from the highly dispersed metal species embedded in the framework [12,13]. Kilos et al. reported on the use of the transition-metal-based metallosilicate NbMCM-41 catalyst in the gas-phase oxidative dehydrogenation of propane and liquid-phase oxidation of cyclohexene [14]. They found that the Lewis acidity, originating from the framework Nb species, was active in both gas and liquid-phase oxidation reactions. Rogovina and Neumann reported promising performance of amorphous cobalt silicate xerogel in the oxidation of ethylbenzene with *tert*-butyl hydroperoxide to acetophenone, where the conversion and selectivity were around 65% and >99%, respectively [15]. Moreover, zeolitic metallosilicates have been proposed as both acid catalysts and efficient supports for metal oxide species. Appropriate post-treatment, such as hydrothermal treatment, can facilitate the dispersion of metal oxide species via internal metal extraction, which leads to potential for promising redox catalysts in the NH_3-SCO [16]. However, excessive treatment conditions may lead to the loss of surface acidity and merely serve as a support. From this perspective, establishing optimal post-hydrothermal treatment conditions that successfully maintain both properties for zeolitic metallosilicate presents a significant challenge.

MWW (**M**CM t**W**enty-t**W**o)-type zeolite is well-known as aluminosilicate MCM-22 in which two-dimensional (2D) MWW layers with sinusoidal 10-ring (4.1 × 5.1 Å) channels parallel to the *x-y* plane are connected in the *z*-axis direction to form three-dimensional (3D) structure with large cylindrical supercages (7.1 Å in diameter and 18.2 Å in height) [17]. A 3D MWW structure can be converted into a 2D MWW by an appropriate but complicated procedure [18]. However, in our previous studies, we developed 3D MWW-type nickel and zincosilicate zeolitic materials, and their 2D delaminated MWW layers (Me-DML, Me = Ni or Zn), through a simple hydrothermal treatment of a borosilicate MWW precursor (B-MWW(P)) with each metal precursor solution [19,20]. It is well known that when comparing with the aluminosilicate, the borosilicate has the advantage to form the vacant sites for the substitution of Me species under the mildly acidic condition of metal precursor solutions mainly due to the shorter atomic radius of B compared to Al [21]. As the hydrothermal temperature increased, the 3D MWW transformed into 2D MWW, and simultaneously, the hetero metal atoms were substituted into the framework, and their content continuously increased. In these studies, we also discovered that these metallosilicates retained Lewis acidity due to the persistence of framework metal species [22]. Highly dispersed metal oxides were formed alongside framework metal species with high metal content in both Ni- and Zn-DMLs when at above 140 °C. These findings suggested that excess metal species could not be incorporated into the framework, likely due to the limited number of available framework vacant sites.

Cobalt oxides can provide superior redox properties to the catalyst, making them effective active metals in the NH_3-SCO reaction [23,24]. Motivated by this, in this study, we prepared 3D and 2D MWW-type cobalt silicates, as well as 2D cobalt phyllosilicates denoted as Co-DML-*x*, through a similar hydrothermal treatment, controlling the synthesis temperatures (*x* = 80–160 °C) as mentioned above [19,20,25]. The structural transformation and Co substitution into the Co-DML frameworks were systematically investigated using various analytical tools. We also analyzed the redox properties and acidities of Co-DMLs, correlating them with their content and chemical states of Co species, respectively. Finally, we demonstrated the bi-functionality of Co-DML catalysts for the NH_3-SCO, and proposed a suitable reaction mechanism.

2. Experimental section

2.1. Synthesis of catalysts

B-MWW(P) with a Si/B ratio of 9.5 was synthesized using hexamethyleneimine (99%, Sigma-Aldrich) as an organic structure-directing agent (SDA) following the previously reported procedure [26]. In a

typical preparation, hexamethyleneimine and sodium hydroxide (99%, Sigma-Aldrich) were dissolved in deionized (DI) water. Subsequently, boric acid (99.5%, Junsei) was added to the mixture at 50 °C. After the dissolution of boric acid, fumed silica (Evonik) was slowly added, and the mixture was homogenized. The final mixture was transferred into a Teflon-lined stainless-steel autoclave and heated at 175 °C for 14 d. After the heating, the solid products were retrieved by filtration with DI water and dried at room temperature (RT).

Co-DML-*x* catalysts were synthesized by a single-step hydrothermal treatment of B-MWW(P) with a 1.0 M cobalt(II) nitrate hexahydrate (98%, Junsei) aqueous solution at 80–160 °C for 4 d with 100 rpm rotation in Teflon-lined stainless-steel autoclaves [19,20]. After the hydrothermal treatment, the solid products were retrieved by filtration with DI water and dried at RT. All the as-synthesized Co-DMLs were calcined at 550 °C for 8 h to remove the remaining organic SDAs before characterization and catalysis.

For comparison, 5 and 20 wt% of Co-impregnated B-MWW catalysts (5 and 20Co/B-MWW, respectively) were prepared using incipient wetness impregnation method with a Co(II) nitrate aqueous solution. After impregnation, the solid was dried at 100 °C and subsequently calcined at 550 °C for 3 h.

2.2. Characterization of catalysts

Powder X-ray diffraction (XRD) patterns were recorded on a Rigaku SmartLab SE X-ray diffractometer with Cu-Kα radiation in the 2θ range from 3° to 50° (scan rate = 4° min^{-1}). The total and external surface areas of the catalysts were characterized by N_2 sorption experiments using a BELSORP mini X. The total surface area was calculated using Brunauer–Emmett–Teller (BET) equation, and the *t*-plot method was used to evaluate the external surface area. Thermogravimetric analysis (TGA) were performed on a Hitachi STA7200 thermal analyzer with air, where the weight losses associated with the combustion of the organic SDAs were additionally confirmed by differential thermal analysis (DTA) on the same analyzer. The elemental compositions were determined using an inductively coupled plasma-optical emission spectrometer (ICP-OES). The $Co_{cluster}/Co_{framework}$ ratios in Table 1 were determined by applying the procedure as follows. The number of tetrahedral framework atoms in the unit cell of MWW structure is 72 [27]. First, we determine the numbers of framework Si and B atoms in B-MWW are 65.2 and 6.8, respectively, based on its Si/B ratio calculated from ICP-OES (Table 1). Next, it was assumed that the number of Si atoms in MWW of our synthesized catalysts was not changed during the hydrothermal treatment used in this study due to the great stability of Si in the framework. Based on this assumption and each Si/Co ratios determined from ICP-OES, we calculated the numbers of framework Co atoms in Co-DML-*x* and Co/B-MWW. Finally, the excess Co atoms noted as $Co_{cluster}$ in Table 1 can be determined by (Si + B + Co) – the total number of atoms in MWW unit cell, i.e., 72.

The IR spectra in the structural region (500–1600 cm^{-1}) were obtained on a Shimadzu IRTracer-100 FT-IR spectrometer in the ATR mode. The IR spectra in the hydroxyl region (OH-IR, 3000–4000 cm^{-1}) were also recorded on the same equipment. A self-supporting solid wafer of approximately 20 mg with 1.3 cm diameter was placed inside a home-built IR cell, pretreated under flowing He (100 mL min^{-1}) at 450 °C for 2 h, and consecutive OH-IR spectra were recorded at the same temperature. Thereafter, to obtain the pyridine-adsorption IR (py-IR) spectra, the sample was cooled to 100 °C and treated with pyridine-saturated dry He for 10 min. Subsequently, flushing with excess He at the same temperature for 30 min removed the physisorbed pyridine. After desorption at 100 °C, the concentrations of the Brønsted (B) and Lewis (L) acid sites were determined from the areas of the IR bands at approximately 1550 and 1450 cm^{-1}, respectively, using the equations of Emeis [28]: concentration of Brønsted acid sites (μmol g^{-1}) = (1.88 × I.A.(B) × R^2)/W × 1000 and concentration of Lewis acid sites (μmol g^{-1}) = (1.42 × I.A. (L) × R^2)/W × 1000, where I.A.(B or L) = the integrated area of the

Table 1
Physicochemical properties of catalysts prepared in this study.

Catalyst[a]	BET surface area (m² g⁻¹)[b]			Chemical composition[c]			Chemical state of Co[f]	
	Total	External	Micropore	Si/B	Co (wt%)[d]	Co$_{cluster}$/Co$_{framework}$[e]	Framework Co	Co$_3$O$_4$
B-MWW	477	25	452	9.5	- (0)	-	-	-
5Co/B-MWW	301	10	291	8.7	4.1 (5)	-	0.0	1.0
Co-DML-80	501	53	448	20.9	4.6 (7)	-	1.0	0.0
Co-DML-100	459	88	371	18.7	5.0 (9)	0.1	1.0	0.0
Co-DML-120	432	142	290	26.1	12.0 (18)	0.5	1.0	0.0
Co-DML-140	337	186	151	41.6	15.1 (28)	0.5	1.0	0.0
Co-DML-160	214	206	8	86.7	23.9 (37)	0.7	0.6	0.4

[a] Calcined in flowing air at 550 °C for 8 h.

[b] Calculated from N$_2$ sorption isotherm data (Fig. S3).

[c] Determined by ICP elemental analysis, unless otherwise stated.

[d] The values in parentheses are determined from STEM-EDS elemental mapping analysis (Fig. 2 and S6).

[e] It is assumed that the number of framework atoms is 72 including 65.2 Si atoms.

[f] The values indicate the relative ratios of the decomposed peak areas of UV-DRS spectra at below and above 300 nm, which indicates the framework Co and Co$_3$O$_4$, respectively (Fig. 3a and S7a).

peaks in IR spectra after pyridine adsorption at around 1550 or 1450 cm⁻¹, R = the radius of the self-supporting wafer (cm), and W = the weight of the self-supporting wafer (g).

UV diffuse reflectance spectroscopy (DRS) was recorded on a Shimadzu UV-2600 UV-Vis spectrophotometer, and the spectra were plotted with the Kubelka–Munk function. X-ray photoelectron spectroscopy (XPS) analysis was conducted using a NEXSA instrument (Thermo Fisher Scientific). The XPS data were carefully calibrated with respect to the binding energy using the 284.8 eV peak corresponding to surface adventitious carbon. The Shirley algorithm was employed to determine the appropriate spectrum boundary conditions. The relative peak ratios were assigned theoretical values of 2:1 and 4:3, respectively, to accurately interpret the spin-orbit characteristics of Co 2p and Si 2p orbitals. The shape and average size of crystal were confirmed by scanning electron microscopy (SEM, Hitachi SU8010, acceleration voltage = 15 kV). (Scanning) transmission electron microscopy ((S)TEM) and energy dispersive spectroscopy (EDS) images were collected using a FEI TALOS F200X operated at 200 kV.

To investigate the redox property and acidity of the catalyst, temperature programmed reduction (TPR) and desorption (TPD) profiles were acquired using a BELCAT II instrument (MicrotacBEL Corp.) equipped with a thermal conductivity detector. The H$_2$-TPR analysis was performed as follows: (a) initial pre-treatment of 0.05 g catalyst at 500 °C for 1 h in a gas flow of 5% O$_2$/Ar, (b) cooling to 100 °C in a pure Ar flow and maintaining this temperature for 30 min to eliminate physically adsorbed O$_2$ on the catalyst, and (c) introduction of a 5% H$_2$/Ar (50 mL min⁻¹) mixture into the gas flow, ramping from 100 °C to 600 °C at a rate of 10 °C min⁻¹. The NH$_3$-TPD procedure involved the following steps: (a) initial pretreatment of 0.05 g catalyst at 500 °C for 1 h in a gas flow of 5% O$_2$/He, (b) cooling to 100 °C in a pure He flow, (c) adsorption of NH$_3$ with 5% NH$_3$/He for 1 h, (d) purging the sample with pure He flow to remove physically adsorbed NH$_3$, and (e) desorption of NH$_3$ from 100 °C to 500 °C with a ramp rate of 10 °C min⁻¹. The NH$_3$-TPR analysis was performed as follows: (a) initial pre-treatment of 0.05 g catalyst at 500 °C for 1 h in a gas flow of 5% O$_2$/He, (b) cooling to 100 °C in a pure He flow and maintaining this temperature for 30 min to eliminate physically adsorbed O$_2$ on the catalyst, and (c) introduction of 1% NH$_3$/He (50 mL min⁻¹) mixture into the gas flow, ramping from 100 °C to 500 °C at a rate of 10 °C min⁻¹. The O$_2$-TPD procedure involved the following steps: (a) initial pretreatment of 0.05 g catalyst at 500 °C for 1 h in a gas flow of pure He, (b) cooling to 100 °C, (c) adsorption of O$_2$ with 5% O$_2$/He for 1 h, (d) purging the sample with pure He flow to remove physically adsorbed O$_2$, and (e) desorption of O$_2$ from 100 °C to 500 °C with a ramp rate of 10 °C min⁻¹. All the spectral decomposition and simulation operations were performed using the Origin 9.0 curve-fitting program.

2.3. Catalysis

The packed-bed reactor tests of the NH$_3$ oxidation were performed using pelletized catalyst sample (30–40 mesh) in a packed-bed reactor. The catalytic performance was evaluated under 500 mL min⁻¹ of continuous gas flow containing 200 ppm NH$_3$, 5% O$_2$, 5% H$_2$O, and balance N$_2$ at a gas hourly space velocity (GHSV) of 100,000 h⁻¹. Furthermore, the catalyst stability evaluation was measured under the same gas composition as mentioned above at 400 °C for 20 h. The catalyst sample was pretreated at 500 °C for 1 h in a flow of 5% O$_2$, 5% H$_2$O, and balance N$_2$ prior to each activity test. The inlet temperature of the catalyst bed was continuously monitored using a thermocouple and served as an indicator of catalyst activity. NH$_3$, N$_2$O, NO and NO$_2$ concentrations were measured using in-situ FT-IR (PerkinElmer Spectrum Two) equipped with a gas cell (PIKE Technologies). The IR spectra were collected at a resolution of 2 cm⁻¹ and 4 times accumulated scans per each point. In addition, NH$_3$-SCR test was evaluated under 500 mL min⁻¹ of continuous gas flow containing 200 ppm NH$_3$, 200 ppm NO, 5% O$_2$, 5% H$_2$O, and balance N$_2$ at 100,000 h⁻¹ GHSV in the same aforementioned IR equipment.

3. Results and discussion

3.1. Synthesis and characterization of Co-DML-x

Fig. 1a shows the powder XRD patterns of Co-DML-x (x = 80–160 °C) catalysts and their parent B-MWW. Co-DML-80 and 100 exhibited the same pattern as B-MWW, representative at 7.4°, 8.1°, 9.9°, and 26.1°, which can be assigned to (100), (101), (102), and (310) reflections of MWW structure, respectively [29]. As the hydrothermal temperature increased from 80 °C to 160 °C, these typical XRD peaks for MWW structure gradually disappeared due to the disordering of 2D delaminated MWW layers. Specifically, Co-DML-160 showed almost no MWW feature, presenting the XRD pattern for 2D cobalt phyllosilicate instead [25,30]. This structural transformation trend aligns with our previous results for Ni- and Zn-DMLs [19,20]. Furthermore, the continuous decrease in the organic SDA content present between the delaminated 2D layers of B-MWW(P) and Co-DML-x with increasing hydrothermal treatment temperature further demonstrates the structural transformation (Fig. 1b and S1). Notably, no XRD peaks corresponding to metallic Co (111), CoO (111) and (200), and Co$_3$O$_4$ (311) and (400) at 44.2°, 36.9°, 42.8°, 37.0°, and 45.0°, respectively, were observed in any of the XRD patterns of Co-DML-x [31–34]. This suggests the high dispersion of Co species and Co substitution in the MWW framework. On the other hand, Co-impregnated 5 and 20Co/B-MWW showed the XRD peaks of Co$_3$O$_4$ alongside the MWW pattern, indicating the formation of sizeable Co$_3$O$_4$ particles on the MWW surface (Fig. S2a). As the cobalt
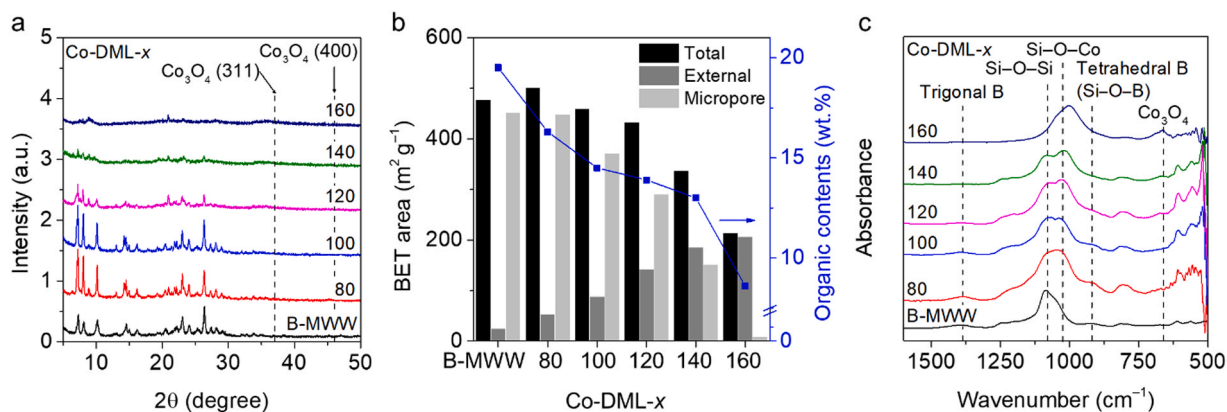
Fig. 1. (a) Powder XRD patterns, (b) BET surface areas and organic content determined by N_2 sorption isotherms and TGA/DTA, respectively, and (c) normalized IR spectra in the structural region of 500–1600 cm^{-1} of Co-DML-*x* (*x* = 80–160 °C). For comparison, those of B-MWW were added.

content of Co/B-MWW increased, the intensity of Co_3O_4 peak also increased, which clearly showed the formation of more Co_3O_4 species in 20Co/B-MWW.

To further investigate the structural transformation phenomena of Co-DML-*x* by increasing the temperature, we obtained their N_2 sorption isotherms (Fig. S3), and the calculated BET surface areas are summarized in Fig. 1b and Table 1. While the N_2 sorption isotherms of Co-DML-80 and 100 exhibited typical type I microporous characters like the patterns of B-MWW and 5Co/B-MWW, those of Co-DML-*x* catalysts were gradually shifted from type I to IV patterns. Moreover, the H3-type hysteresis loops became more pronounced from Co-DML-120–160. This originates from the interparticle void volumes between disordered 2D layers [35]. The gradual change of crystal morphology from the agglomerate of plate-like crystals of Co-DML-80 to the heavily overlapped thin plates of Co-DML-160 supported the structural transformation (Fig. S4). In correlation, B-MWW exhibited a distinct specific surface area of a 3D MWW structure, where the micropore area was approximately 20 times higher than its external surface area. Conversely, the external surface areas of Co-DML-*x* gradually increased with the elevation of the hydrothermal temperature due to further delamination of MWW. Co-DML-140 revealed an external surface area approximately 20 times greater than its micropore area, likely attributable to its almost fully delaminated 2D MWW character. Remarkably,

Co-DML-160 showed almost no micropore characteristic owing to its 2D amorphous cobalt phyllosilicate layers. The total specific surface areas of Co-DML-*x* gradually decreased with increasing temperature, with Co-DML-160 being only ca. 44% compared to B-MWW, which is probably owing to the exceptionally high Co content in Co-DML-160 (ca. 24 wt%, Table 1).

To investigate the substitution of framework Co species and the structural transformation, the Co-DML-*x* catalysts were analyzed by IR spectroscopy in the structural region of 500–1600 cm^{-1}. As shown in Fig. 1c, B-MWW exhibited the characteristic IR absorption bands for MWW-type borosilicate at 569, 611, 809, 1080, 1183, 1243, and 1398 cm^{-1} [36]. The IR bands at 569 and 611 cm^{-1} correspond to the deformable vibration of tetrahedral units for –O–Si–O– and/or –O–B–O– and double rings in MWW structure, respectively. The intensities of these two IR bands decreased with increasing hydrothermal temperature, and finally, these two MWW characteristic bands almost disappeared in Co-DML-160, supporting the formation of amorphous cobalt phyllosilicate. This is consistent with the powder XRD and N_2 sorption results, as discussed above. Therefore, we can conclude that the structures of Co-DML-*x* were changed from 3D to 2D MWW, and further 2D amorphous layer of cobalt phyllosilicate as shown in Scheme 1a. By the way, the IR band at 1080 cm^{-1} can be attributed to Si–O–Si bond, and the bands at 937 and 1403 cm^{-1} are assignable to tetra- and
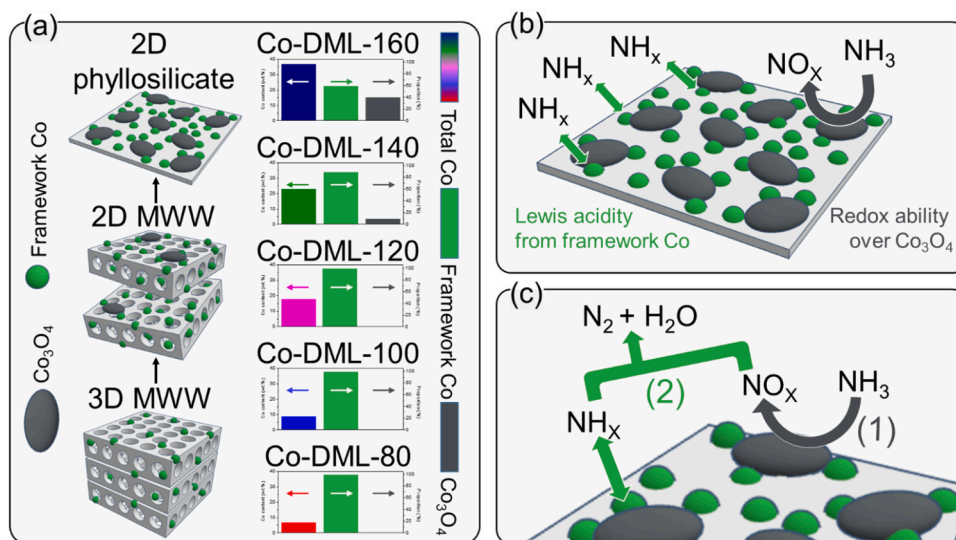
Scheme 1. (a) Structural transformation from 3D to 2D (left) and change of chemical composition and state of Co in Co-DML-*x* by increasing the hydrothermal temperature x = 80–160 °C, (b) bi-functionality of Co-DML-160, and (c) suggested reaction mechanism as *i*-SCR in NH₃-SCO over Co-DML-160: (1) excessive oxidation and (2) selective reduction.

tri-coordinated framework B species [37]. Interestingly, the intensities of these three IR bands for framework Si and B species decreased. In contrast, the framework Si–O–Co intensity appeared at 1025 cm^{-1} gradually increased with the elevation of hydrothermal temperature [38], indicating the simultaneous substitution of Co species instead of the framework B species. Notably, Co-DML-140 and 160 showed the additional IR band for Co_3O_4 at 661 cm^{-1}, the identical peak confirmed in cobalt-impregnated B-MWW (5 and 20Co/B-MWW; Fig. S2b). Co-DML-160 showed the most pronounced IR bands for both framework Si–O–Co and Co_3O_4, likely due to the coexistence of cobalt phyllosilicate and Co_3O_4 on the 2D layer external surface [39].

Fig. 2 presents the (S)TEM-EDS images of B-MWW and Co-DML-*x* catalysts. As increasing hydrothermal temperature, delamination progresses as thick plate-shaped crystals of B-MWW were converted to thin delaminated plates of overlapped 2D layers as observed in SEM images (Fig. S4). In the Co elemental mapping image, the Co content increased from 7 wt% (Co-DML-80) to 37 wt% (Co-DML-160), the trend which also corresponded well with ICP elemental analysis results (Table 1). All the Co species, both framework Co and Co_3O_4, were significantly well-dispersed, even in Co-DML-160 crystallite. Small but noticeable agglomerated Co species were also observed on the surface of Co-DML-*x* with exception of Co-DML-80, potentially due to Co clusters surrounded by framework Co species (Fig. S5). When comparing the ratios of $Co_{cluster}/Co_{framework}$, as estimated from ICP elemental analysis, the values increased from 0.1 (Co-DML-100) to 0.7 (Co-DML-160) (Table 1). On the other hand, 5 and 20Co/B-MWW exhibited the significantly agglomerated Co species even in 5Co/B-MWW despite its much lower Co content (ca. 4 wt%) compared to Co-DML-*x* (Fig. S6 and Table 1).

In addition, when compared to our previously reported Ni- and Zn-DML-*x* materials, the Co content in Co-DML-*x* was slightly higher than those of Ni and Zn at the same hydrothermal temperature (e.g., ca. 3 wt % of Ni and Zn in Ni- and Zn-DML-100 based on ICP analysis) [19,20]. This can be explained by the higher acidity of the Co precursor solution (pH ∼ 3) than those (pH ∼ 4) of the Ni and Zn precursor solutions, which can enhance the B extraction and subsequently increase the Co substitution. Note that the structural transformation of three Co-, Ni-, and Zn-DML metallosilicates were quite similar. Based on these results, two separate kinetic schemes for structural transformation and metal substitution can be differentiated even though the two phenomena occur during the same crystallization process. This separation of kinetics is also demonstrated in our previously reported interzeolite transformation of B-MWW to metallosilicate BEA-type zeolites by hydrothermal treatment with different metal (Co, Ni, and Zn) precursor solutions [40].

UV-DRS measurements were conducted to examine the chemical states of Co species in Co-DML-*x* catalysts. As depicted in Fig. 3a, while B-MWW without Co species did not show any UV absorption peak, all the Co-DML-*x* catalysts exhibited the UV absorption peaks below 300 nm, which can be attributed to the charge transfer from O^{2-} to Co^{2+} in the framework [41,42]. The intensities of these UV absorption peaks gradually increased with the rise in the hydrothermal temperature, except for Co-DML-100, which was less intense compared to Co-DML-80. We confirmed the same analytical results for the samples obtained from repeated synthesis. As summarized in Table 1, unlike Co-DML-80, Co-DML-100 was calculated to have 0.1 Co cluster per framework Co. Thus, this might be probably due to the shielding effect of Co cluster on framework Co in Co-DML-100. On the other hand, Co-DML-160 demonstrated a significant UV absorption for framework
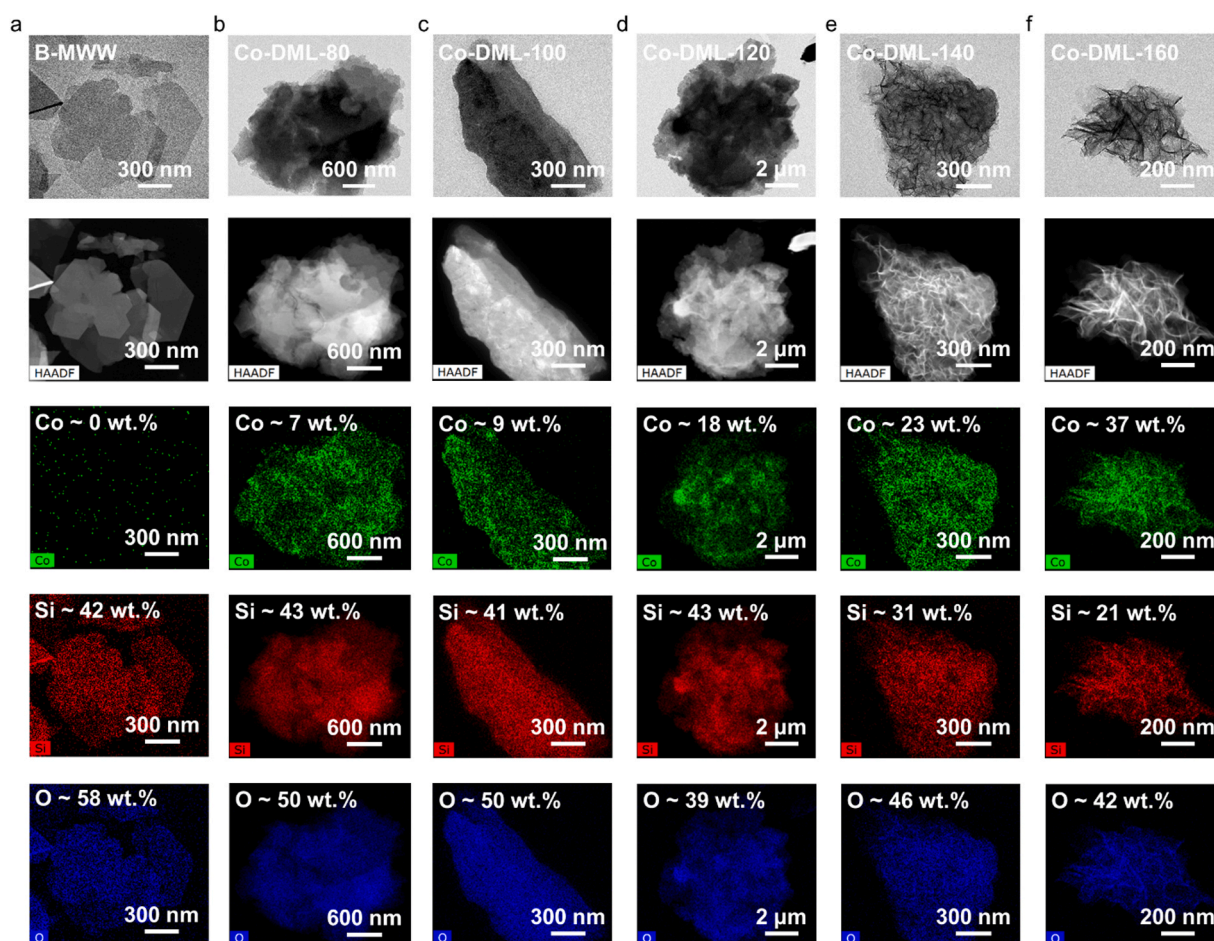

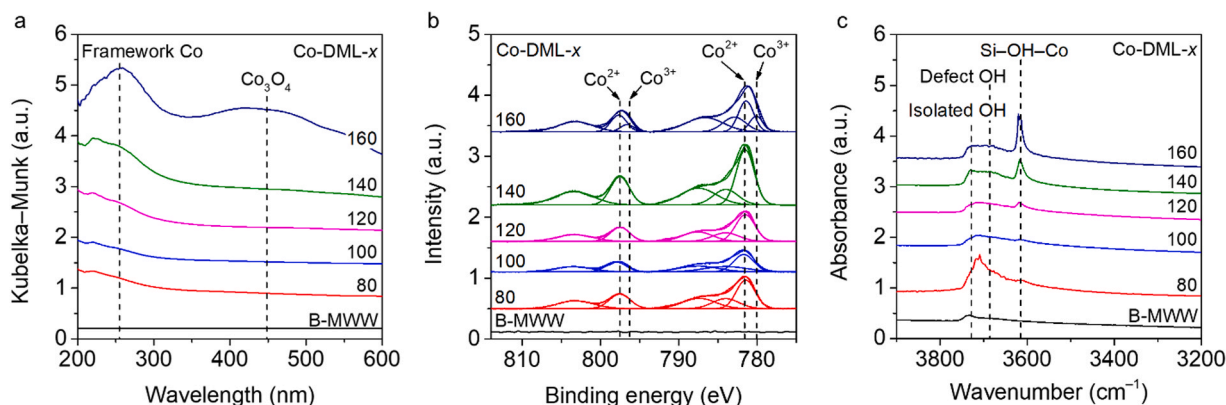**Fig. 2.** TEM and STEM-EDS elemental mapping images of (a) B-MWW and (b–f) Co-DML-*x* (*x* = 80–160 °C).

Fig. 3. (a) UV-DRS spectra, (b) Co 2p XPS spectra, and (c) IR spectra in the hydroxyl region of 3200–4000 cm^{-1} of Co-DML-x (x = 80–160 °C). For comparison, those of B-MWW were added.

Co species among Co-DML-x catalysts and an additional wide UV band in the range of 400–600 nm, which can be assigned to extra-framework Co_3O_4 species with a relative proportion of approximately 0.6:0.4 (Table 1) [43]. However, both the 5 and 20Co/B-MWW samples showed a marginal UV absorption band for Co_3O_4 (Fig. S7a), and the 20Co/B-MWW contained relatively more Co_3O_4. These observations are in good agreement with the IR spectra in the structural region, as discussed in Fig. 1c.

Fig. 3b shows the Co 2p XPS spectra of B-MWW and Co-DML-x catalysts. Generally, the Co 2p XPS spectra can be distinguished into two binding energies, i.e., Co $2p_{3/2}$ and Co $2p_{1/2}$, along with their shake-up satellites at around 784–787 and 803 eV, respectively [44,45]. The discussion herein is based on Co $2p_{3/2}$, as the trend observed in Co $2p_{1/2}$ closely resembles all samples. The Co $2p_{3/2}$ can be further classified into two types of XPS peaks depending on their chemical states, i.e., Co^{2+} and Co^{3+} at around 781.5 and 780.0 eV, respectively [46,47]. Although the framework Co species has one XPS peak of Co^{2+}, the Co_3O_4 with a normal spinel structure containing octahedral Co^{3+} and tetrahedral Co^{2+} in a 2:1 ratio should exhibit two XPS peaks [47,48]. Only one XPS peak was observed in Co-DML-80–140 but was assignable to the framework Co^{2+} species with increasing intensities except for Co-DML-100. Similar to the UV-DRS results (Fig. 3a), the intensity of Co-DML-100 was lower than that of Co-DML-80. Conversely, Co-DML-160 showed two Co $2p_{3/2}$ peaks related to Co^{2+} and Co^{3+} in 3.7:1.3 ratio, which is corresponding to its UV-DRS result. Additionally, the positions of Si 2p XPS peaks for Co-DML-x gradually decreased with increasing the Co content (Fig. S8), further indicating the existence of Si–O–Co in Co-DML-x [49]. 5Co/B-MWW also displayed two Co $2p_{3/2}$ XPS peaks attributable to Co^{2+} and Co^{3+} of Co_3O_4 (Fig. S7b), as the position of its Si 2p XPS peak is similar to that of B-MWW without Co species (Fig. S7c) and UV-DRS result of 5Co/B-MWW also indicate only existence of Co_3O_4 (Fig. S7a). Thus, based on the comprehensive structural IR, UV-DRS, and XPS results, the change in chemical states of Co species in Co-DML-x catalysts can be summarized as illustrated in Scheme 1a, i.e., framework Co in Co-DML-80–120 and framework Co + Co_3O_4 in Co-DML-140 and 160.

Fig. 3c displays the OH-IR spectra in the range of 3200–4000 cm^{-1} for B-MWW and Co-DML-x. B-MWW exhibited a relatively lower intensity but clearly showed some resolved characteristic bands, i.e., isolated silanol, silanol groups interacting with hydrogen bonding in defect sites (defective silanol), and $OB(OH)_2$ at 3732–3684 cm^{-1} [50,51]. In the case of Co-DML-x, an additional IR band corresponding to Si–OH–Co was observed at 3614 cm^{-1} [52], distinct from B-MWW. The intensity of this peak gradually increased with increasing hydrothermal temperature, providing evidence for the successful substitution of Co in the DML structure. Furthermore, 5Co/B-MWW did not show any of this IR band for Si–OH–Co due to the absence of framework Co species (Fig. S7d).

Interestingly, Co-DML-80 showed the highest intensities of IR peaks for silanol groups among the Co-DML-x catalysts studied here. This indicates that the hydrothermal energy at 80 °C is sufficient to remove the framework atoms but insufficient to promote Co substitution into the framework.

3.2. Bi-functional properties of Co-DML-x

The redox and acidic properties of the Co-DML-x catalysts can be manipulated based on the structural transformation from 3D to 2D, the increase of Co content in the DML framework, and the formation of Co_3O_4 species on the external surface with increasing hydrothermal temperature as discussed above. First, the redox properties of Co-DML-x catalysts were explored with H_2-TPR analysis. As shown in Fig. 4a, while only a weak and broad peak at around 320 °C was observed in Co-DML-100 and 120, the two resolved H_2 consumption peaks centered at 300 and 350 °C were featured in Co-DML-80. These two intense reductions may be originated from the unreduced framework oxygen (–O–Si–O$^-$) formed at the perturbed defect sites resulting from the extraction of tetrahedral atom [53,54]. This correlated well with the high intensity of silanol defect sites discussed in OH-IR for this catalyst (Fig. 3c). In Co-DML-140, on the other hand, a broad peak with a slight increase in intensity was observed at around 360 °C, and significantly broader and stronger reduction peaks, about 5 times higher intensity than that of Co-DML-140, were found in a wide range of 200–450 °C in Co-DML-160. Since Co/B-MWW containing agglomerated Co_3O_4 cannot exhibit such enhanced redox properties (Fig. S9a), highly dispersed Co_3O_4 in the 2D layered cobalt phyllosilicate significantly contributes to the improved redox property. The tendency for H_2 consumption appearing from lower temperatures (starting from 200 °C; Co-DML-160) can offer a distinct advantage in NH$_3$-SCO performances.

The acidic properties of Co-DML-x were analyzed by py-IR spectroscopy (Fig. 4b and S10) and NH$_3$-TPD (Fig. 4c), with the results also summarized in Table S1. The py-IR spectrum of B-MWW with Si/B = 9.5 did not show any acidity (Fig. S11 and Table S1), which suggests that the framework B species in the Co-catalysts prepared in this study do not have the effect on their acidities. As shown in Fig. 4b, Co-DML-80 exhibited the highest Brønsted acid concentration, mainly due to the large number of silanol groups among the Co-DML-x catalysts, as discussed in Fig. 3c [55]. However, as the hydrothermal temperature increased from 80 °C to 160 °C, the concentration of Brønsted acid sites gradually decreased, and the Lewis acids increased in Co-DML-x, finally Co-DML-160 had only a B/L ratio of 0.03. Transition-metal based metallosilicates normally contain Lewis acid sites associated with the framework-bound metal species [56,57]. 5Co/B-MWW also showed the high Lewis acidity, but it was lower than that of Co-DML-160 (Fig. S9b). As shown in Fig. 4c, the NH$_3$-TPD profiles showed broad peaks for all
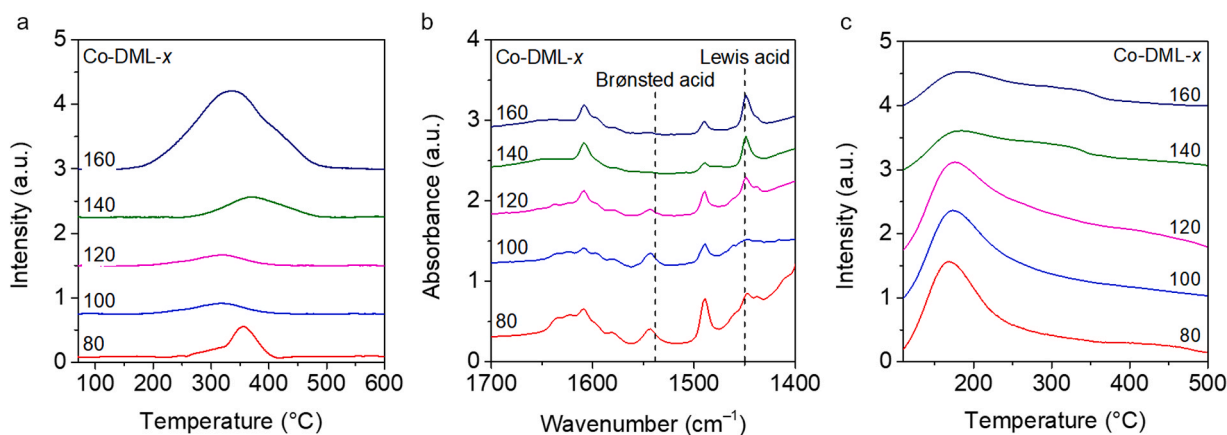
Fig. 4. (a) H$_2$-TPR curves, (b) IR spectra after pyridine adsorption at 100 °C, and (c) NH$_3$-TPD profiles of Co-DML-*x* (*x* = 80–160 °C).

Co-DML-*x* catalysts. Interestingly, a distinct change in the NH$_3$ desorption peaks was observed with increasing hydrothermal temperature. The peaks at below 200 °C were dominant in Co-DML-80–120, whereas the formation of stronger acid sites at higher than 300 °C was observed in Co-DML-140 and 160 catalysts. In the py-IR spectra measured with increasing temperature from 100 °C to 450 °C (Fig. S10), Co-DML-160 showed the strongest acidic strength among the Co-DML-*x* catalysts as shown that the pyridine chemisorption peak was observed even until 450 °C (Fig. S10e), which is corresponding to the NH$_3$-TPD result. These py-IR and NH$_3$-TPD results of Co-DML-160 are due to the significantly existing framework Co species (ca. 14 wt%) even with Co$_3$O$_4$ (ca. 10 wt %) (Table 1). However, 5Co/B-MWW did not show strong acid sites, as confirmed by NH$_3$-TPD (Fig. S9c) and py-IR (Fig. S10f). From the

comparison of acidic characterizations between 5Co/B-MWW and Co-DML-*x*, it can be concluded that abundant framework cobalt played a critical role to strengthen acidity. Thus, Co-DML-160 can be utilized as the bi-functional catalyst with the strong redox ability and Lewis acidity as illustrated in Scheme 1b.

3.3. Catalytic activity of Co-DML-x in NH$_3$-SCO

Fig. 5a,b and S12 shows the overall catalytic NH$_3$-SCO performances of Co-DML-*x* and 5Co/B-MWW catalysts, with the corresponding results also summarized in Table S2. As compared in Fig. 5a, the enhancement of catalytic NH$_3$ oxidation over Co-DML-*x* exactly followed the trend of redox ability and Lewis acidity of Co-catalysts studied here (Fig. 4).
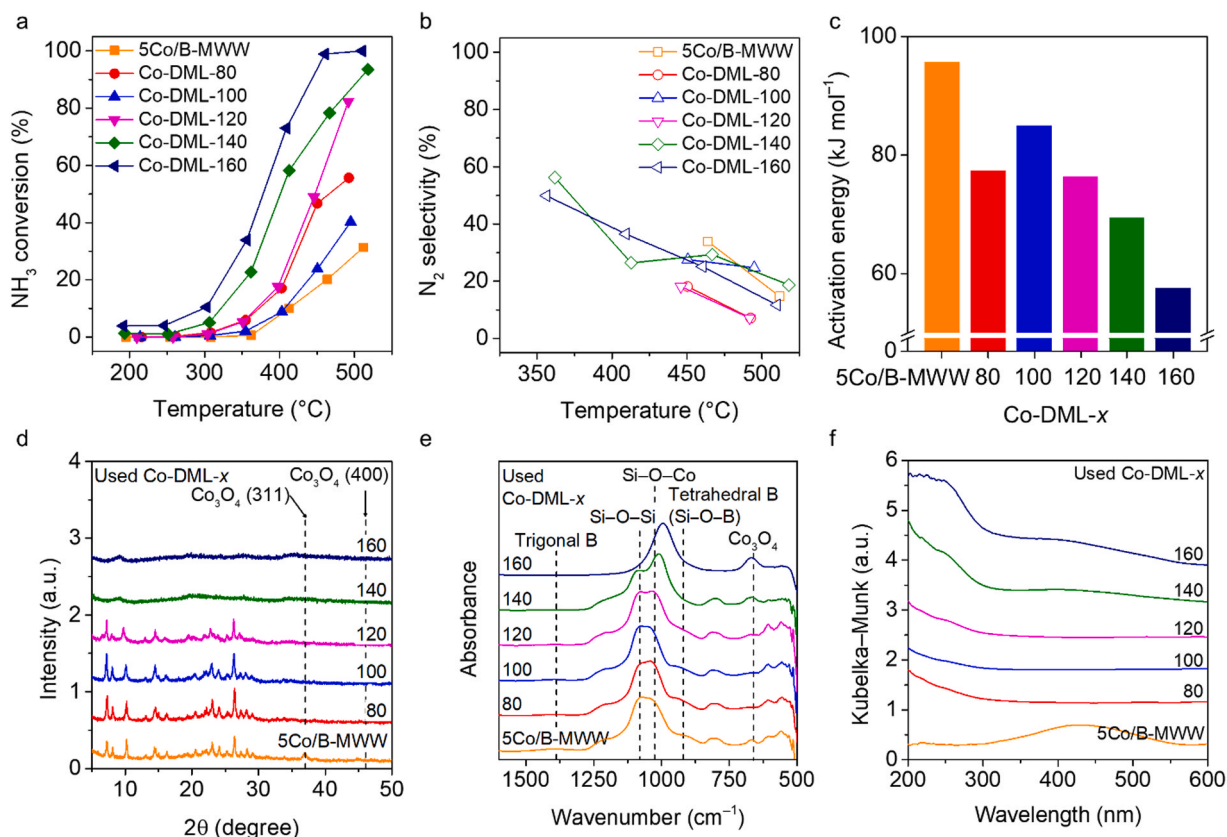

Fig. 5. (a) NH$_3$ conversion, (b) N$_2$ selectivity, and (c) calculated activation energy over 5Co/B-MWW and Co-DML-*x* (*x* = 80–160 °C) in NH$_3$-SCO at 200–500 °C. (d) Powder XRD patterns, (e) IR spectra in the structural region of 500–1600 cm^{-1}, and (f) UV-DRS spectra of the spent Co-DML-*x* catalysts after NH$_3$-SCO. For comparison, those of used 5Co/B-MWW were added.

Notably, Co-DML-160 demonstrated the highest NH_3 oxidation conversions at all reaction temperatures, reaching approximately 99% at 450 °C. This result can be rationalized by the synergic effect of the dual functionality, i.e., highly dispersed Co_3O_4 for the redox ability and framework Co for the Lewis acidity. On the other hand, 5Co/B-MWW demonstrated the lowest NH_3 conversions at all reaction temperatures compared to Co-DML-*x*, probably due to the relatively weak redox ability and mild acidity. This can be attributed to the agglomerated Co_3O_4 serving as the sole active component in 5Co/B-MWW. The benefit of the Co-DML catalysts can be further discussed through the N_2 selectivity shown in Fig. 5b. The N_2 selectivity was calculated only from data with ammonia conversion above 20% [58]. The most abundant by-product formed was NO, while the formation of N_2O and NO_2 was negligible (Fig. S12). Catalysts prepared at low hydrothermal temperature conditions (Co-DML-80–120), even including 5Co/B-MWW catalysts, showed low N_2 selectivity of ~30% above 400 °C. On the other hand, Co-DML-140 and 160 catalysts synthesized under high hydrothermal temperature conditions showed high N_2 selectivity, more than 50% at 350 °C. The enhanced N_2 selectivity can be attributed to the aforementioned surface acidity. These two catalysts facilitate stronger interactions with NH_3 by presenting more substantial Lewis acid sites from their significantly formed framework Co species (Table 1), favoring N_2 formation reaction rather than excessive NH_3 oxidation to by-products [59,60]. Considering the amount of cobalt loaded, 20Co/B-MWW shows relatively higher NH_3 conversion than Co-DML-160 as shown in Fig. S13. However, the 20Co/B-MWW cannot form N_2 while oxidizing NH_3. This marginal N_2 selectivity of 20Co/B-MWW, but superior N_2 selectivity underscores the bi-functional role of the two active sites in Co-DML-160 over NH_3-SCO reaction. Additionally, when comparing the Co-DML-160 with the previously reported catalysts for NH_3-SCO [61–64], Co-DML-160 exhibited the comparable NH_3 conversion, but the N_2 selectivity was not necessarily higher than those of other catalysts (Table S3). Nevertheless, we suggest that the bi-functionality of Co-DML-160 catalyst including redox ability and the chemisorption of NH_3 can improve the NH_3-SCO performance.

The activation energies of Co-catalysts for this NH_3-SCO are also estimated and summarized in Fig. 5c. The activation energies for the NH_3 oxidation over Co-catalysts exhibited the following trend: 5Co/B-MWW (95.74 kJ mol^{-1}) > Co-DML-100 (85.04 kJ mol^{-1}) > Co-DML-80 (77. 47 kJ mol^{-1}) > Co-DML-120 (76.51 kJ mol^{-1}) > Co-DML-140 (69.52 kJ mol^{-1}) > Co-DML-160 (57.65 kJ mol^{-1}), which correlated well with the catalytic performance. The activation energy varied depending on the types of Co phases, i.e., framework Co and Co_3O_4, of Co-DML-*x* and 5Co/B-MWW at different hydrothermal treatment temperatures as proved by aforementioned characterization results. As a result, the lowest activation energy of Co-DML-160 also support the synergic effect of crucial two catalytic properties, surface acidity and redox property, on activity in NH_3-SCO reaction.

From the overall reaction results with the redox ability and Lewis acidity, the internal selective catalytic reduction (*i*-SCR) mechanism can be suggested in this case (Scheme 1c) [12,59,60]. According to this mechanism, the first step is the excess oxidation of NH_3 to NO_x on Co_3O_4. The second step entails the selective reduction of NO_x on the interface of Co_3O_4 and framework Co by the residual NH_x primarily chemisorbed on Lewis acidic framework Co sites. To better understand the NH_3-SCO mechanism, we performed O_2-TPD and NH_3-TPR experiments for evaluating O_2 activation and NH_3 activation abilities, respectively, of the three catalysts, i.e., Co-DML-100, Co-DML-160, and 5Co/B-MWW, which had different types of Co species as mentioned above, i.e., framework Co for Co-DML-100, framework Co and Co_3O_4 for Co-DML-160, and Co_3O_4 for 5Co/B-MWW. As shown in Fig. S14a, while the O_2-TPD results did not show significant differences between the catalysts, in NH_3-TPR (Fig. S14b), Co-DML-160 exhibited the two more resolved peaks at higher temperatures compared to the other two catalysts, indicating its unique catalytic properties for NH_3 activation, which is consistent with the NH_3-SCO activity. Thus, we believe that

NH_3 activation is a key step for the NH_3-SCO reaction. In addition, we tested the NH_3-SCR activity of the Co-DML-160 and 5Co/B-MWW catalysts as shown in Fig. S15. When comparing between Co-DML-160 and 5Co/B-MWW, Co-DML-160 catalyst showed the superior NO conversion and corresponding N_2 selectivity in NH_3-SCR reaction, which could be the direct evidence for suggesting that *i*-SCR mechanism performed in NH_3-SCO reaction in this study. Additionally, the 2D structural character of Co-DML-160 could be another contributor to the highest NH_3 conversions because the 2D layers could allow for greater exposure of its Co species, including framework Co and Co_3O_4, to the reactants as well as the efficient diffusion of products.

Fig. 5d–f shows the characterization data for the used Co-DML-*x* and 5Co/B-MWW catalysts after the NH_3-SCO reaction. As shown in Fig. 5d, the used Co-DML-*x* catalysts still did not show any XRD peaks for Co_3O_4, indicating the preservation of framework Co species in the frameworks and highly dispersed Co_3O_4. On the other hand, the used 5Co/B-MWW still showed the XRD peaks corresponding to agglomerated Co_3O_4. Even though the used Co-DML-140 showed the enhanced powder XRD pattern of cobalt phyllosilicate, this Co-DML-140 still exhibited the weak but clear IR peaks for MWW structure at around 560 and 610 cm^{-1} with more intensified IR peak for Co_3O_4 compared to its pristine Co-DML-140 (Fig. 5e). This indicates that the catalyst was partially transformed to cobalt phyllosilicate during the reaction. Nonetheless, Co-DML-*x* catalysts retained the chemical states of Co species in each catalyst after the NH_3-SCO reaction as shown in UV-DRS (Fig. 5f) and the IR spectra in the structural region. Furthermore, the long-term stability evaluation results shown in Fig. S16 demonstrate the stable catalytic activities of Co-DML-*x* catalysts over NH_3-SCO reaction.

4. Conclusions

We synthesized Co-DML catalysts via a direct hydrothermal treatment of B-MWW(P) with Co precursor solution at different temperatures. By only adjusting the hydrothermal temperature, Co-DML structures were transformed from 3D to 2D MWW layers and finally to 2D phyllosilicate, and the Co content in Co-DML also increased from ca. 5–24 wt%. Notably, the in-situ change of chemical states of Co species in Co-DML was observed as follows: framework Co (Co-DML-80, 100, and 120) into framework Co + Co_3O_4 (Co-DML-140 and 160). Particularly, Co-DML-160 exhibited the formation of ca. 40% Co_3O_4 and 60% framework Co, which resulted in the efficient bi-functional catalyst with the strongest redox and the highest Lewis acid sites among the catalysts prepared in this study. In line with its promising physicochemical property, Co-DML-160 showed a high NH_3 conversion (~99% at 450 °C) with the lowest activation energy (57.65 kJ mol^{-1}) and the high N_2 selectivity (>50% at 350 °C) in the NH_3-SCO. The hydrothermal synthesis of cobalt silicate can serve as a versatile synthetic strategy allowing for the structural transformation and metal substitution and the development of new bi-functional metallosilicate catalysts.

CRediT authorship contribution statement

Siyeon Lee: Data curation, Formal analysis, Investigation, Writing – original draft. **Sang Woo Byun:** Data curation, Formal analysis, Investigation, Writing – original draft. **Sungjoon Kweon:** Investigation, Writing – original draft. **Hyeonwoo Shin**: Data curation, Formal analysis. **Hyung-Ki Min:** Conceptualization, Formal analysis. **Min Bum Park:** Conceptualization, Funding acquisition, Supervision, Writing – review & editing. **Sung Bong Kang:** Conceptualization, Funding acquisition, Supervision, Writing – review & editing.

Declaration of Competing Interest

The authors declare that they have no known competing financial interests or personal relationships that could have appeared to influence the work reported in this paper.

Data availability

Data will be made available on request.

Acknowledgements

Appendix A. Supporting information

Supplementary data associated with this article can be found in the online version at doi:10.1016/j.apcatb.2023.123264.

References

[1] M.E. Davis, R.J. Davis. Fundamentals of chemical reaction engineering, 1st edition., McGraw Hill, New York, USA, 2003.

[2] L. Zhang, M. Zhou, A. Wang, T. Zhang, Selective hydrogenation over supported metal catalyst: from nanoparticles to single atoms, Chem. Rev. 120 (2020) 683–733, https://doi.org/10.1021/acs.chemrev.9b00230.

[3] K.S. Go, S.R. Son, S.D. Kim, Reaction kinetics of reduction and oxidation of metal oxides for hydrogen production, Int. J. Hydrogen Energy 33 (2008) 5986–5995, https://doi.org/10.1016/j.ijhydene.2008.05.039.

[4] E.T.C. Vogt, B.M. Weckhuysen, Fluid catalytic cracking: recent developments on the grand old lady of zeolite catalysis, Chem. Soc. Rev. 44 (2015) 7342, https://doi.org/10.1039/C5CS00376H.

[5] A.M. Robinson, J.E. Hensley, J.W. Medlin, Bifunctional catalysts for upgrading of biomass-derived oxygenates: a review, ACS Catal. 6 (2016) 5026–5043, https://doi.org/10.1021/acscatal.6b00923.

[6] J.W. Bae, S.-H. Kang, Y.-J. Lee, K.-W. Jun, Synthesis of DME from syngas on the bifunctional Cu–ZnO–Al₂O₃/Zr-modified ferrierite: effect of Zr content, Appl. Catal. B 90 (2009) 426–435, https://doi.org/10.1016/j.apcatb.2009.04.002.

[7] L. Chmielarz, M. Jabłońska, Advances in selective catalytic oxidation of ammonia to dinitrogen: a review, RSC Adv. 5 (2015) 43408, https://doi.org/10.1039/C5RA03218K.

[8] D. Macina, A. Opioła, M. Rutkowska, S. Basąg, Z. Piwowarska, M. Michlik, L. Chmielarz, Mesoporous silica materials modified with aggregated transition metal species (Cr, Fe and Cr-Fe) in the role of catalysts for selective catalytic oxidation of ammonia to dinitrogen, Mater. Chem. Phys. 187 (2017) 60, https://doi.org/10.1016/j.matchemphys.2016.11.047.

[9] L. Xu, C. Wang, H. Chang, Q. Wu, T. Zhang, J. Li, New insight into SO₂ poisoning and regeneration of CeO₂–WO₃/TiO₂ and V₂O₅–WO₃/TiO₂ catalysts for low-temperature NH₃–SCR, Environ. Sci. Technol. 52 (2018) 7064, https://doi.org/10.1021/acs.est.8b01990.

[10] M. Jabłońska, A. Król, E. K.-Zajac, K. Tarach, L. Chmielarz, K. G.-Marek, ZeoliteY modified with palladium as effective catalyst for selective catalytic oxidation of ammonia to nitrogen, J. Catal. 316 (2014) 36–46, https://doi.org/10.1016/j.jcat.2014.04.022.

[11] F. Wang, J. Ma, G. He, M. Chen, S. Wang, C. Zhang, H. He, Synergistic effect of TiO₂–SiO₂ in Ag/Si–Ti catalyst for the selective catalytic oxidation of ammonia, Ind. Eng. Chem. Res. 57 (2018) 11903–11910, https://doi.org/10.1021/acs.iecr.8b02205.

[12] L.I. Darvell, K. Heiskanen, J.M. Jones, A.B. Ross, P. Simell, A. Williams, An investigation of alumina-supported catalysts for the selective catalytic oxidation of ammonia in biomass gasification, Catal. Today 81 (2003) 681–692, https://doi.org/10.1016/S0920-5861(03)00166-4.

[13] J. Přech, Catalytic performance of advanced titanosilicate selective oxidation catalysts – A review, Catal. Rev. 60 (2018) 71–131, https://doi.org/10.1080/01614940.2017.1389111.

[14] B. Kilos, M. Aouine, I. Nowak, M. Ziolek, J.C. Volta, The role of niobium in the gas- and liquid-phase oxidation on metallosilicate MCM-41-type materials, J. Catal. 224 (2004) 314–325, https://doi.org/10.1016/j.jcat.2004.03.002.

[15] M. Rogovin, R. Neumann, Silicate xerogels containing cobalt as heterogeneous catalysts for the side-chain oxidation of alkyl aromatic compounds with *tert*-butyl hydroperoxide, J. Mol. Catal. A 138 (1999) 315–318, https://doi.org/10.1016/S1381-1169(98)00207-6.

[16] J.B. Lim, S.H. Cha, S.B. Hong, Direct N₂O decomposition over iron-substituted small-pore zeolites with different pore topologies, Appl. Catal. B 243 (2019) 750–759, https://doi.org/10.1016/j.apcatb.2018.10.068.

[17] M.E. Leonowicz, J.A. Lawton, S.L. Lawton, M.K. Rubin, MCM-22: a molecular sieve with two independent multidimensional channel systems, Science 264 (1994) 1910–1913, https://doi.org/10.1126/science.264.5167.1910.

[18] A. Corma, V. Fornes, S.B. Pergher, Th.L.M. Maesen, J.G. Buglass, Delaminated zeolite precursors as selective acidic catalysts, Nature 396 (1998) 353–356, https://doi.org/10.1038/24592.

[19] H.-K. Min, S. Kweon, Y.W. Kim, H. An, D. Jo, E.D. Park, C.-H. Shin, M.B. Park, Atomically dispersed nickel species in a two-dimensional molecular sieve: Origin of high activity and stability in dry reforming of methane, Appl. Catal. B 298 (2021) 120627, https://doi.org/10.1016/j.apcatb.2021.120627.

[20] H.-K. Min, S. Kweon, S. Oh, H. An, Y. Cho, H. Min, D. Jo, J.F. Kim, C.-H. Shin, S. B. Kang, M.B. Cho, Single-step preparation of zinco- and aluminosilicate delaminated MWW layers for the catalytic conversion of glucose, Green Chem. 23 (2021) 9489–9501, https://doi.org/10.1039/D1GC02353E.

[21] X. Ouyang, S.-J. Hwang, R.C. Runnebaum, D. Xie, Y.-J. Wanglee, T. Rea, S.I. Zones, A. Katz, Single-step delamination of a MWW borosilicate layered zeolite precursor under mild conditions without surfactant and sonication, J. Am. Chem. Soc. 136 (2014) 1449–1461, https://doi.org/10.1021/ja410141u.

[22] S. Kweon, S. Lee, J.H. Lee, M.B. Park, Comparative study of interzeolite transformed metallosilicates for the chemisorption of benzene, toluene, and xylenes, Appl. Surf. Sci. 612 (2023), 155851, https://doi.org/10.1016/j.apsusc.2022.155851.

[23] N.I. Il'chenko, Catalytic oxidation of ammonia, Russ. Chem. Rev. 45 (1976) 1119, https://doi.org/10.1070/RC1976v045n12ABEH002765.

[24] M. Jabłońska, Al.M. Robles, A comparative mini-review on transition metal oxides applied for the selective catalytic ammonia oxidation (NH₃-SCO), Materials 15 (2022) 4770, https://doi.org/10.3390/ma15144770.

[25] H.-K. Min, H. Min, S. Kweon, Y.W. Kim, S. Lee, C.-H. Shin, M.B. Park, S.B. Kang, Selective hydrogenation of CO₂ to CH₄ over two-dimensional nickel silicate molecular sieves, Catal. Sci. Technol. 12 (2022) 2232–2240, https://doi.org/10.1039/D2CY00103A.

[26] R. Millini, G. Perego, W.O. Parker, G. Bellussi, L. Carluccio, Layered structure of ERB-1 microporous borosilicate precursor and its intercalation properties towards polar molecules, Microporous Mater. 4 (1995) 221–230, https://doi.org/10.1016/0927-6513(95)00013-Y.

[27] C. Baerlocher, L.B. McCusker, Database of Zeolite Structures, http://www.iza-structure.org/database/.

[28] C.A. Emeis, Determination of integrated molar extinction coefficients for infrared absorption bands of pyridine adsorbed on solid acid catalysts, J. Catal. 141 (1993) 347–354, https://doi.org/10.1006/jcat.1993.1145.

[29] W.J. Roth, D.L. Dorset, Expanded view of zeolite structures and their variability based on layered nature of 3-D frameworks, Microporous Mesoporous Mater. 142 (2011) 32–36, https://doi.org/10.1016/j.micromeso.2010.11.007.

[30] J.S. Kim, I. Park, E.-S. Jeong, K. Jin, W.M. Seong, G. Yoon, H. Kim, B. Kim, K. T. Nam, K. Kang, Amorphous cobalt phyllosilicate with layered crystalline motifs as water oxidation catalyst, Adv. Mater. 29 (2017), 1606893, https://doi.org/10.1002/adma.201606893.

[31] X. Yuan, X.-X. Hu, X.-L. Ding, H.-C. Kong, H.-D. Sha, H. Lin, W. Wen, G. Shen, Z. Guo, Z.-F. Ma, Y. Yang, Effects of cobalt precursor on pyrolyzed carbon-supported cobalt-polypyrrole as electrocatalyst toward oxygen reduction reaction, Nanoscale Res. Lett. 8 (2013) 478, https://doi.org/10.1186/1556-276X-8-478.

[32] D. Barreca, C. Massignan, S. Daolio, M. Fabrizio, C. Piccirillo, L. Armelao, E. Tondello, Composition and microstructure of cobalt oxide thin films obtained from a novel cobalt(II) precursor by chemical vapor deposition, Chem. Mater. 13 (2001) 588–593, https://doi.org/10.1021/cm001041x.

[33] L.J. Garces, B. Hincapie, R. Zerger, S.L. Suib, The effect of temperature and support on the reduction of cobalt oxide: an in situ X-ray diffraction study, J. Phys. Chem. C 119 (2015) 5484–5490, https://doi.org/10.1021/jp5124184.

[34] X. Cheng, D. Su, Z. Wang, C. Ma, M. Wang, Catalytic reduction of nitrogen oxide by carbon monoxide, methane and hydrogen over transition metals supported on BEA zeolites, Int. J. Hydrog. Energy 43 (2018) 21969–21981, https://doi.org/10.1016/j.ijhydene.2018.09.206.

[35] M. Rutkowska, U. Díaz, A.E. Palomares, L. Chmielarz, Cu and Fe modified derivatives of 2D MWW-type zeolites (MCM-22, ITQ-2 and MCM-36) as new catalysts for DeNOₓ process, Appl. Catal. B 168–169 (2015) 531–539, https://doi.org/10.1016/j.apcatb.2015.01.016.

[36] M. Yan, F. Jin, Y. Ding, G. Wu, R. Chen, L. Wang, Y. Yan, Synthesis of titanium-incorporated MWW zeolite by sequential deboronation and atom-planting treatment of ERB-1 as an epoxidation catalyst, Ind. Eng. Chem. Res. 58 (2019) 4764–4773, https://doi.org/10.1021/acs.iecr.8b05836.

[37] B. Qiu, F. Jiang, W.-D. Lu, B. Yan, W.-C. Li, Z.-C. Zhao, A.-H. Lu, Oxidative dehydrogenation of propane using layered borosilicate zeolite as the active and selective catalyst, J. Catal. 385 (2020) 176–182, https://doi.org/10.1016/j.jcat.2020.03.021.

[38] L. Wang, E. Guan, Y. Wang, L. Wang, Z. Gong, Y. Cui, X. Meng, B.C. Gates, F.-S. Xiao, Silica accelerates the selective hydrogenation of CO₂ to methanol on cobalt catalysts, Nat. Commun. 11 (2020) 1033, https://doi.org/10.1038/s41467-020-14817-9.

[39] G. St, M. Christoskova, M. Stoyanova, D. Georgieva, Mehandjiev, Preparation and characterization of a higher cobalt oxide, Mater. Chem. Phys. 60 (1999) 39–43, https://doi.org/10.1016/S0254-0584(99)00053-X.

[40] S. Kweon, Y. Cho, D. Jo, H.-K. Min, M.B. Park, Interzeolite transformation of borosilicate MWW to metallosilicate BEA-type zeolites: Separated kinetics of structural transformation and metal substitution, Chem. Mater. 35 (2023) 4717–4730, https://doi.org/10.1021/acs.chemmater.3c00438.

[41] X. Dong, Y. Yu, Y. Zhang, Z. Xu, H. Jiang, C. Meng, C. Huang, Synthesis of cobalt silicate nanosheets with mesoporous structure and high surface area as the promising electrode for high-performing hybrid supercapacitor, Electrochim. Acta 380 (2021), 138225, https://doi.org/10.1016/j.electacta.2021.138225.

[42] Q. Wang, Y. Zhang, H. Jiang, X. Li, Y. Cheng, C. Meng, Designed mesoporous hollow sphere architecture metal (Mn, Co, Ni) silicate: a potential electrode material for flexible all solid-state asymmetric supercapacitor, Chem. Eng. J. 362 (2019) 818–829, https://doi.org/10.1016/j.cej.2019.01.102.

[43] S. Faisal, F.A. Jan, S. Saleem, R. Ullah, N.Ullah Wajidullah, Salman, *Juglans regia L.* mediated synthesis of cobalt oxide and zinc-doped cobalt oxide nanoparticles: Characterization and evaluation for environmental, antibacterial and cytotoxic potential, Nanotechnol. Environ. Eng. 7 (2022) 675–689, https://doi.org/10.1007/s41204-022-00252-2.

[44] J.L. Gautier, E. Rios, M. Gracia, J.F. Marco, J.R. Gancedo, Characterisation by X-ray photoelectron spectroscopy of thin $Mn_xCo_{3-x}O_4(1 \geq x \geq 0)$ spinel films prepared by low-temperature spray pyrolysis, Thin Solid Films 311 (1997) 51–57, https://doi.org/10.1016/S0040-6090(97)00463-X.

[45] D.-T. To, Y.-C. Chiang, J.-F. Lee, C.-L. Chen, Y.-C. Lin, Nitrogen-doped Co catalyst derived from carbothermal reduction of cobalt phyllosilicate and its application in levulinic acid hydrogenation to γ-valerolactone, Catal. Lett. 152 (2022) 2090–2100, https://doi.org/10.1007/s10562-021-03784-5.

[46] M.A. Salim, E.E. Khawaja, X-ray photoelectron spectroscopy study of sodium germanate glass containing cobalt oxide, J. Non-Cryst. Solids 151 (1992) 71–80, https://doi.org/10.1016/0022-3093(92)90011-8.

[47] M. Domínguez, E. Taboada, H. Idriss, E. Molins, J. Llorca, Fast and efficient hydrogen generation catalyzed by cobalt talc nanolayers dispersed in silica aerogel, J. Mater. Chem. 20 (2010) 4875–4883, https://doi.org/10.1039/C0JM00184H.

[48] K.P. Reddy, R. Jain, M.K. Ghosalya, C.S. Gopinath, Metallic cobalt to spinel Co_3O_4—electronic structure evolution by near-ambient pressure photoelectron spectroscopy, J. Phys. Chem. C 121 (2017) 21472–21481, https://doi.org/10.1021/acs.jpcc.7b06661.

[49] J. Cañón, A.V. Teplyakov, XPS characterization of cobalt impregnated SiO_2 and γ-Al_2O_3, Surf. Interface Anal. 53 (2021) 475–481, https://doi.org/10.1002/sia.6935.

[50] D. Meloni, S. Laforge, D. Martin, M. Guisnet, E. Rombi, V. Solinas, Acidic and catalytic properties of H-MCM-22 zeolites: 1. Characterization of the acidity by pyridine adsorption, Appl. Catal. A 215 (2001) 55–66, https://doi.org/10.1016/S0926-860X(01)00501-4.

[51] Y. Gong, M. Zhou, Matrix isolation infrared spectroscopic and theoretical study of the hydrolysis of boron dioxide in solid argon, J. Phys. Chem. A 112 (25) (2008) 5670–5675, https://doi.org/10.1021/jp8014172.

[52] E.M. Flanigen, H. Khatami, H.A. Szymanski, Infrared structural studies of zeolite frameworks, Adv. Chem. 101 (1971) 201–229, https://doi.org/10.1021/ba-1971-0101.ch016.

[53] I.C. Medeiros-Costa, E. Dib, N. Nesterenko, J.-P. Dath, J.-P. Gilson, S. Mintova, Silanol defect engineering and healing in zeolites: Opportunities to fine-tune their properties and performances, Chem. Soc. Rev. 50 (2021) 11156, https://doi.org/10.1039/D1CS00395J.

[54] G. Brunklaus, H. Koller, S.I. Zones, Defect models of as-made high-silica zeolites: clusters of hydrogen-bonds and their interaction with the organic structure-directing agents determined from ^{1}H double and triple quantum NMR spectroscopy, Angew. Chem. Int. Ed. 55 (2016) 14459–14463, https://doi.org/10.1002/anie.201607428.

[55] V. Siozios, M. Hunger, M.R. Hansen, H. Koller, Disentangling Brønsted acid sites and hydrogen-bonded silanol groups in high-silica zeolite H-ZSM-5, J. Phys. Chem. C 124 (2020) 23380–23386, https://doi.org/10.1021/acs.jpcc.0c06113.

[56] B. Tang, W. Dai, X. Sun, G. Wu, N. Guan, M. Hungerb, L. Li, Mesoporous Zr-Beta zeolites prepared by a post-synthetic strategy as a robust Lewis acid catalyst for the ring-opening aminolysis of epoxides, Green Chem. 17 (2015) 1744, https://doi.org/10.1039/C4GC02116A.

[57] R. Baran, L. Valentin, S. Dzwigaj, Incorporation of Mn into the vacant T-atom sites of a BEA zeolite as isolated, mononuclear Mn: FTIR, XPS, EPR and DR UV-Vis studies, Phys. Chem. Chem. Phys. 18 (2016) 12050, https://doi.org/10.1039/C6CP01713D.

[58] S.W. Byun, S.J. Lee, M. Kim, W.B. Bae, H. Shin, M.J. Hazlett, D. Kang, B. Tesfaye, P.W. Park, S.B. Kang, High N_2 selectivity of Pt-V-W/TiO_2 oxidation catalyst for simultaneous control of NH_3 and CO emissions, Chem. Eng. J. 444 (2022), 136517, https://doi.org/10.1016/j.cej.2022.136517.

[59] T. Lan, Y. Zhao, J. Deng, J. Zhang, L. Shi, D. Zhang, Selective catalytic oxidation of NH_3 over noble metal-based catalysts: state of the art and future prospects, Catal. Sci. Technol. 10 (17) (2020) 5792–5810, https://doi.org/10.1039/D0CY01137A.

[60] L. Chmielarz, P. Kuśtrowski, M. Drozdek, R. Dziembaj, P. Cool, E.F. Vansant, Selective catalytic oxidation of ammonia into nitrogen over PCH modified with copper and iron species, Catal. Today 114 (2006) 319–325, https://doi.org/10.1016/j.cattod.2006.01.020.

[61] C.-M. Hung, Application of Pt-Rh complex catalyst: feasibility study on the removal of gaseous ammonia, Int. J. Phys. Sci. 7 (2012) 2166, https://doi.org/10.5897/IJPS12.024.

[62] R.Q. Ling, R.T. Yang, Superior ion-exchanged ZSM-5 catalysts for selective catalytic oxidation of ammonia to nitrogen, Chem. Commun. (2000) 1651–1652, https://doi.org/10.1039/B004957N.

[63] Y. Li, J.N. Armor, Selective NH_3 oxidation to N_2 in a wet stream, Appl. Catal. B 13 (1997) 131, https://doi.org/10.1016/S0926-3373(96)00098-7.

[64] A. Akah, C. Cundy, A. Garforth, The selective catalytic oxidation of NH_3 over Fe-ZSM-5, Appl. Catal. B 59 (2005) 221, https://doi.org/10.1016/j.apcatb.2004.10.020.